SCIENCE CHINA
Physics, Mechanics & Astronomy

• Article •

July 2016 Vol. 59 No. 7: 674711
doi: 10.1007/s11433-016-0115-1

Lateral migration of dual droplet trains in a double spiral microchannel†

ChunDong Xue[1,2], XiaoDong Chen[1], Chao Liu[1,2], and GuoQing Hu[1,2*]

[1] *State Key Laboratory of Nonlinear Mechanics, Beijing Key Laboratory of Engineered Construction and Mechanobiology, Institute of Mechanics, Chinese Academy of Sciences, Beijing 100190, China;*
[2] *School of Engineering Science, University of Chinese Academy of Sciences, Beijing 101408, China*

Received March 25, 2016; accepted April 12, 2016; published online May 17, 2016

Microfluidic droplets have emerged as novel platforms for chemical and biological applications. Manipulation of droplets has thus attracted increasing attention. Different from solid particles, deformable droplets cannot be efficiently controlled by inertia-driven approaches. Here, we report a study on the lateral migration of dual droplet trains in a double spiral microchannel at low Reynolds numbers. The dominant driving mechanism is elucidated as wall effect originated from the droplet deformation. Three types of migration modes are observed with varying Reynolds numbers and the size-dependent mode is intensively investigated. We obtain empirical formulas by relating the migration to Reynolds numbers and droplet sizes. The effect of droplet deformability on the migration and the detailed migration behavior along the double spiral channel are discussed. Numerical simulations are also performed and yielded in qualitative agreement with the experiments. This proposed low *Re* approach based on lateral migration could be a promising alternative to existing inertia-driven approaches especially concerning deformable entities and susceptible bio-particles.

microfluidics, droplet, migration, double spiral microchannel

PACS number(s): 47.61.-k, 47.55.D-, 47.57.ef

Citation: C. D. Xue, X. D. Chen, C. Liu, and G. Q. Hu, Lateral migration of dual droplet trains in a double spiral microchannel, Sci. China-Phys. Mech. Astron. **59**, 674711 (2016), doi: 10.1007/s11433-016-0115-1

1 Introduction

The emergence of microfluidic droplets offers new opportunities for chemical and biological researches and has raised extensive attention [1-4]. Droplets can be used to provide microscale and independent compartments for reaction [5], to encapsulate cells for detection [6,7], and to enrich and transport particles [8,9]. Manipulation of droplets in microfluidic device is of fundamental and practical significance.

The last decade has seen extensive development of microfluidic approaches for particle/cell manipulation by either active methods using external force fields [10-14] or passive methods depending on hydrodynamic forces [15-17]. More recently, inertial migration has been increasingly involved for manipulation of rigid particles by hydrodynamic forces [18-20]. The inertial lift on a rigid particle stems from the asymmetry of pressure and viscous stresses on the particle surface in a Poiseuille flow at infinite Reynolds numbers ($Re > 1$, and $Re = \rho U_m L / \eta$, where ρ and η are the density and viscosity of the carrier fluid, respectively, U_m the mean channel velocity, and L the channel characteristic length) [16,20,21]. In contrast to rigid particles, the droplets can

*Correspondence author (email: guoqing.hu@imech.ac.cn)
†Recommended by YouShi Hong (Associate Editor-in-Chief)

experience cross-stream migration even at much lower *Re* ($Re < 1$) due to their deformability [22-24]. The deformability-induced effects influence the migration behavior and manifold the equilibrium positions, resulting in poor performance of inertial manipulation of the droplets [17]. Our previous study shows that two extra equilibrium positions for droplet exist near the channel centerline caused by the deformation, in addition to the widely recognized Segré-Silberberg equilibrium positions caused by the inertia [25].

The driving force behind the low *Re* migration is attributed to the introduction of nonlinearity by droplet deformation [26]. The deformed droplet breaks the laminar and time-reversible regime of low *Re* flow and causes the non-uniform velocity profile and pressure distribution nearby [27]. These asymmetries then give rise to a lift force to induce the cross-stream migration that is generally directed away from the adjacent wall [23,28]. This wall effect is minimum at channel centerline while increases with droplet getting closer to the wall [29,30].

The wall effect can play a dominant role in the migration of deformable entities in shear flow at low *Re* [18,29,31]. After closely positioning droplets near wall by sheath fluid, it is possible to realize separation by sizes in the downstream flow. Maenaka et al. [32] demonstrated this size-dependent separation scheme for binary droplets in a pinched channel. Geislinger et al. [33] exploited the separation of red blood cells from other blood components in a simple T-shaped channel. Using the same channel, sorting of the circulating MV3-melanama cells from suspension of red blood cells was also achieved [34]. In most of the existing studies, strong side flow is required and only one wall works at low *Re,* thus limiting the sample throughputs. If both walls of the microchannel contribute, the throughput and efficiency could be improved significantly. Moreover, introduction of asymmetrical channel structure can also produce lift forces in simple systems [20]. Curved structures like serpentine or spiral have been frequently employed to improve the performance of inertial manipulation of rigid particles [16,35,36]. For droplets in low *Re* flows, curved channels would also influence the migration behaviour, which is rarely addressed in existing studies.

Therefore, in the present work, we explore the lateral migration of dual droplet trains in a double spiral microchannel at low *Re*. The set of droplet train is to eliminate hydrodynamic interactions among droplets in the transverse direction and thus to realize a deterministic manner of cross-stream migration. The effects of *Re* numbers, droplet sizes and deformability on the droplet migration are investigated. The migration behavior of the dual droplet trains in the double spiral channel is investigated in details. We additionally performed numerical simulations to understand droplet dynamics in the curved channels at low *Re*. Sorting based on this lateral migration could be a promising alternative to existing inertial-driven approaches especially for manipulation of deformable entities and susceptible bio-particles.

2 Material and method

2.1 Experimental

2.1.1 Design and material

The employed microchip is composed of a double T (DT) structure and a 2-loop double spiral (DS) channel (Figure 1(a)). The DT structure [37,38], designed with two side inlets for the droplet phases and one intermediate inlet for the continuous phase, is able to synchronously generate dual droplet trains near the two walls, respectively (Figures 1(b) and a1 in Appendix). The flow rates of the two droplet phases are always adjusted to be equal, allowing adequate time to stabilize, and yield the dual droplet trains with equal sizes and frequencies. The continuous phase is also used as the carrier fluid and drives the droplet trains into the DS channel. The DS channel first rotates in the clockwise direction for two loops, changes the direction by an inverted S-shaped junction, and then rotates in the counter-clockwise direction for another two loops. The spacing between two adjacent loops is 800 μm. The four channel curvature radii (R) are 400, 1600, 2800 and 4000 μm, respectively, from inner to outer. The cross section of channel is 400 μm in width (w) and 100 μm in height (h), and the channel width w is used as the channel characteristic length L.

The droplet phase is pure water with density and viscosity of 1 g/cm^3 and 1 mPa·s, respectively. Olive oil is chosen as the

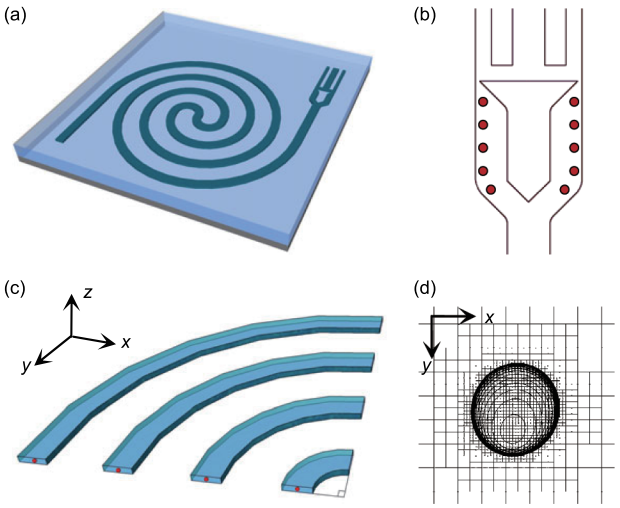

Figure 1 (Color online) (a) The schematic of the microchip. (b) The double T structure for droplet generation. The two side inlets are used for introducing droplet phases and the intermediate inlet for continuous phase. The red circles represent the droplets. (c) The schematic of computational domains. Quarters of circumference are considered. The red solid spheres represent the droplets. (d) The grid of the droplet and the ambient fluid. To get high-resolution simulation, the grid near the interface is refined using gradient-based and thickness-based adaptive mesh refinement technique.

continuous phase with density of 0.92 g/cm^3 and viscosity of 78 mPa·s. The interfacial tension σ between the pure olive oil and the pure water is measured as (20.3±0.08) mN/m using the pendant droplet method (Theta, Attension Inc., Switzerland). In contrast experiments, Tween20, a nonionic surfactant, is added to decrease the interfacial tension and thus increase the droplet deformability. The interfacial tension after adding 0.8% (v/v) Tween20 is measured as (1.3±0.06) mN/m. All the experiments are carried at the room temperature.

2.1.2 Microchip fabrication and experimental operation

The microchip is fabricated in polydimethylsiloxane (PDMS) based on the standard soft-lithography technique [39]. The SU8-3050 master mold of channel structure on a silicon wafer is fabricated first (CapitalBio, China). PDMS is mixed in a ratio of 10:1 with the curing agent and degassed in a vacuum vessel, and then cast over the fabricated wafer and baked in oven at 70°C for 3 h. The PDMS mold is then diced and peeled from the wafer. Three inlets and one outlet are punched using the steel needle with a flattened tip. Plastic tubes are subsequently inserted into the four ports and sealed with adhesive glue (3145 RTV, Dow Corning Inc., USA). The chip is baked again and then bonded with a glass substrate (25 mm × 75 mm) after oxygen plasma treatment (Plasma cleaner; Harrick Inc., USA). The whole thickness of the assembled chip is about 0.8 mm (Figure a1). The chip is finally placed in oven at 80°C for overnight to restore the material to its native hydrophobic condition.

In experiments, the microchip is mounted on the stage of an inverted microscope (Nikon Eclipse Ti, Nikon Instruments Inc., Japan). Three syringe pumps (Pump 11 Elite, Harvard apparatus Inc., USA) are used to introduce fluid phases into channel, i.e., two outer inlets for the droplet phase and one inner inlet for the continuous phase, respectively. The images are recorded using a high-speed CCD camera (Phantom v7.3, Vision Research Inc., USA) and the Phantom Camera Control software (Pcc2.14). With a fixed 9 μs exposure time, the videos are taken at 100-1000 fps (frames per second) depending on the *Re* numbers. The captured images are then processed using Adobe Photoshop CS2 and analyzed using ImageJ software package (National Institute of Health, USA). The time-series images (200 frames) are stacked using *z*-projection with standard deviation and the pseudo-colour of magenta is added.

2.2 Numerical

Direct numerical simulations (DNS) of the two-phase interfacial flow are also performed using the Gerris flow solver [40] to further understand the droplet dynamics in curved channels. The computational domain is simplified to quarter of circumstance for each curvature (Figure 1(c)). Boundary conditions are set as constant axial velocity at the inlet, outflow condition at the outlet, and no-slip conditions on all the walls. A thickness-based refinement method combining with the gradient-based refinement is applied on the interfaces to improve the computational efficiency (Figures 1(d) and a2 in Appendix) [41]. Simulations are first performed without droplets to obtain steady flow fields. Spherical droplets are then placed at different width positions to flow freely with the continuous fluid. When the quasi-static state is achieved, the acceleration of a droplet is calculated from the quadratic differential of the lateral displacement. More details about the numerical simulations are provided in Appendix.

3 Results and discussion

3.1 Experimental

3.1.1 Three migration modes of the dual droplet trains

Through adjusting the flow rates of the two droplet phases synchronously or the continuous phase alone, droplets with different diameters a in varying Re numbers can be obtained. The droplets are generally kept in dual ordered trains close to the two walls at the inlets, respectively. We then observe the droplet distributions at the downstream and outlets. By examining various experiments (Re = 0.063-0.63), three migration modes with varying Re are summarized. First, when channel flow is very slow (Re = 0.063-0.1), the dual ordered trains cannot be kept and the droplets always fall into disorder. Second, in larger flow rate regime (Re = 0.13-0.38), the dual droplet trains change to be robust and can keep ordered all along the channel. Third, as the flow rate further increases (Re = 0.45-0.63), the dual droplet trains tend to focus into one train, regardless of the droplet sizes. The experimental snapshots and the corresponding stacked images with pseudo-colour of magenta are grouped in three panels successively in Figure 2, clearly demonstrating the three migration modes.

In the first mode, the disordered droplet distributions are attributed to the insufficient inertia and the Dean mixing effect of the DS structure [42,43]. This can be predicted from the ratio of the magnitudes of inertial lift force and Dean drag force though they both are very weak. The theoretical formulas for inertial lift force and Dean drag force can be expressed in eqs. (1) and (2) [16], and the ratio β is immediately obtained in eq. (3), where x represents droplet position in channel width.

$$F_{L,i} = \frac{\rho U_{\mathrm{m}}{}^2 a^4}{w^2} f(Re, x), \tag{1}$$

$$F_D \sim \rho U_{\mathrm{m}}{}^2 a w^2 R^{-1}, \tag{2}$$

$$\beta = \frac{F_{L,i}}{F_D} \sim \left(\frac{a}{w}\right)^3 \left(\frac{R}{w}\right) f(Re, x). \tag{3}$$

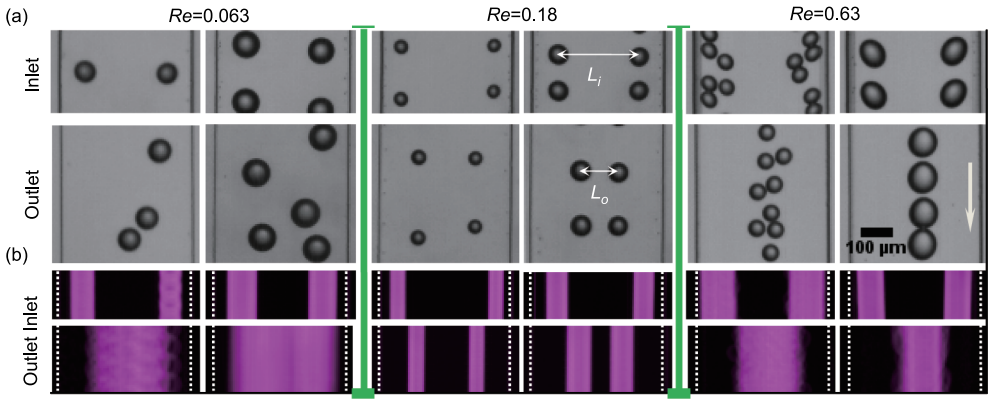

Figure 2 (Color online) (a) Experimental snapshots of the droplet distributions at the inlets and the outlets in the three typical *Re* flow. At each *Re*, conditions of droplets with two sizes are compared. (b) The corresponding stacked images with the pseudo-color of magenta successively grouped. In the second panel with $Re = 0.18$, L_i and L_o denote the lateral distances between the two droplet trains at the inlet and the outlet, respectively. The white arrow indicates the flow direction.

Considering channel width w is 400 μm, radius R is between 400-4000 μm, droplet diameter a is not larger than 100 μm and the coefficient of inertial lift force $f(Re,x) \ll 1$ [18], $F_D \gg F_{L,i}$ is obtained. The Dean effect tends to mixes the droplets especially in the innermost inverted S-shaped channel where the radius R is smallest. As *Re* increases, in the second mode, the Dean drag force is partly offset by the inertial force. The droplets, therefore, can always keep in dual ordered trains though with inward migration. This migration is dominated by the deformation-induced force and the magnitude of migration also depends on *Re* numbers and droplet sizes. As *Re* further increases, in the third mode, the droplet deformation is more prominent so that the droplets are driven toward the channel center by the enhanced deformation-induced force [22,29,44], and ultimately focused into one train. Although the large number density of small droplet influences the focusing, the focusing positions with different droplet sizes are nearly identical (i.e., $x = 0.55w$).

3.1.2 *The size-dependent migration*

The second mode migration is attractive to us because it exhibits the size-dependent behavior that raises the potential of size-dependent separation of droplets or other deformable entities in our proposed channel. To quantitatively investigate migration of this mode, we introduce the migration factor as $\varepsilon = L_m / L_i$, where $L_m = L_i - L_o$ is net migration length, and, L_i and L_o represent the lateral distances between the dual droplet trains at the inlet and the outlet, respectively, as defined in Figure 2.

In Figure 3(a), the red circles represent the experimental results at $Re = 0.13$-0.38, and the black solid line is best fit to them. Therefore, the dependence of migration factors on the *Re* numbers and the droplet sizes a can be described by a linear function:

$$\varepsilon = Re\left(73\frac{a}{w} - 3.4\right). \tag{4}$$

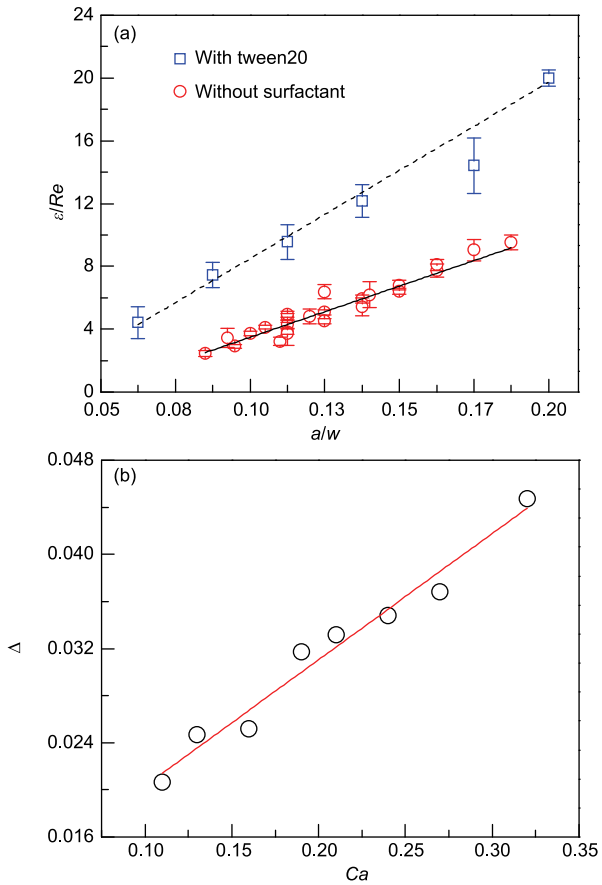

Figure 3 (Color online) (a) The dependence of the migration factors on the *Re* numbers and the droplet sizes. The red circles represent the experimental data at $Re = 0.13$-0.38 in pure olive oil while the blue squares represent the results at $Re = 0.13$ under the Tween20 laden condition. The error bars represent the uncertainty of the measurements. (b) The plot exhibits a linear dependence of droplet deformation parameters on the capillary numbers. All straight lines are the best fits to the corresponding experimental data.

This empirical formula also predicts that the focusing of the dual trains would be size-independent if *Re* numbers are large enough, which agrees with our observation of the third mode migration behavior. The blue squares in Figure 3(a) represent

the experimental results for Tween20 laden olive oil, which will be discussed in another section below.

Moreover, the droplet deformation in a channel flow is determined by the balance between shear force experienced by the droplet and the droplet surface tension, characterized by the capillary number, $Ca = \eta U_m / \sigma$. The deformation can be described by the Taylor's deformation parameter [45] $\Delta = (T-S)/(T+S)$, where T and S are the longest and shortest axes of an appropriate elliptical droplet, respectively. Figure 3(b) shows that Δ depends linearly on Ca at the inlets, i.e., $\Delta \propto Ca$. Due to the high viscosity of the olive oil η and the low interfacial tension σ in our experiments, the Ca numbers are rather large even at low Re numbers. The droplet deformation thus plays a dominant role in regulating the migration.

The deformation-induced lift force is related positively to the Ca numbers and negatively to the separations between the droplets and the channel walls, according to the theoretical prediction by Chan and Leal [46] as well as empirical suggestion by Stan et al. [44]. In the present experiments, the droplets are initially placed very close to the channel walls and therefore the deformation and the deformation-induced lift force are maximized. As the droplets migrate away from the channel walls, the wall effect and the deformation-induced force both decrease while another wall-directed force caused by shear gradient increases. They reach a balance at the equilibrium positions between the walls and the channel center [16,47]. On that account, the droplets still behave in two ordered trains but with decreased lateral distances.

In the migration process of the dual droplet trains, decreasing lateral distance between the two trains may increase the interaction of two trains and weaken the inward migration. We first generate the single-left and single-right droplet train separately to exclude the stream-stream interaction (Figure 4(a)). Such operation allows us to directly compare the migration process between the dual trains and the single train. Nearly identical results are observed at Re = 0.13 (Figure 4(b)), indicating that the interaction between two synchronous trains is negligible and has little influence on the migration of each train. Because of the high viscosity ratio and the low Re regime, the water droplets in each train only perturb the flow around themselves at a small scale. For larger droplets at larger Re number, the interaction will be slightly intensified. Therefore, the weak train-train interaction can allow further migration of larger droplets and focusing of the dual droplet trains, which will be demonstrated later.

3.1.3 *Transition from migration to focusing*

In the second mode, if Ca is further increased, either by increasing the Re number or by decreasing the droplet surface tension σ, the focusing of the droplets into one train could be achieved as the result of the enhanced dominating deformation-induced lift force. Increasing the Re numbers will generate a size-independent focusing pattern that is classified as the third mode. Here, we lower the droplet surface tension by adding 0.8% (v/v) Tween20, and demonstrate the migration to focusing with varying droplet sizes at Re = 0.13.

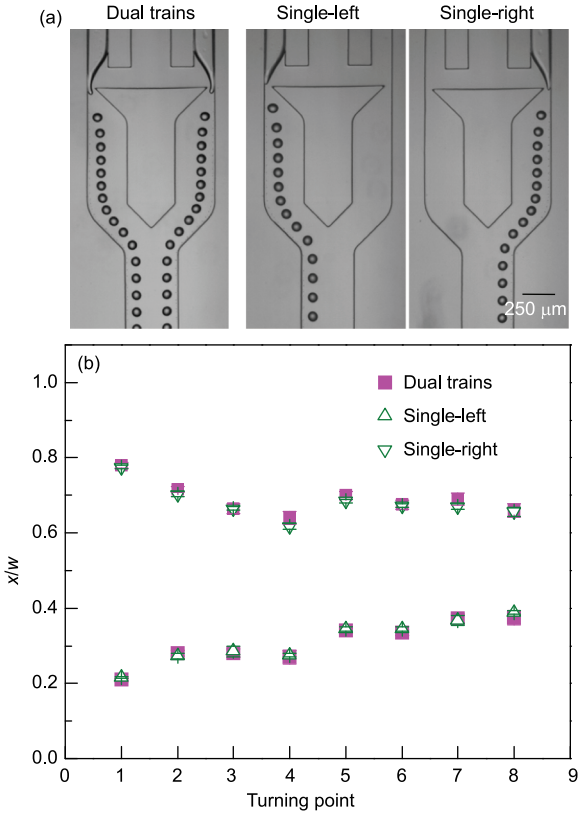

Figure 4 (Color online) (a) Experimental snapshots depict the generation of the dual droplet strains and the generation of single-left as well as single-right droplet train at Re = 0.13. (b) The droplet positions for the two corresponding cases along the DS channel. The data are captured at the eight turning points along the whole DS channel.

Figure 5 demonstrates the transition from migration to focusing under the Tween20 laden condition with the increasing droplet sizes. In this scenario with low Re and high Ca, the lift force caused by the shear gradient is weak, and the deformation-induced lift force can dominate the migration to focus the large droplets into one train. Quantitatively, a linear function similar to the eq. (4) that relates the migration factor to Re and a under the Tween20 laden condition can also be obtained, as described by the black dashed line in Figure 3(a):

$$\varepsilon = Re\left(112\frac{a}{w} - 2.7\right). \quad (5)$$

Comparing eqs. (4) and (5), we acknowledge that the migration efficiency of the droplets in Tween 20 laden flow increases by about fifty percent in contrast to the droplets in pure olive oil, as a result of the increased deformability.

Figure 6 exhibits the varying Δ along the DS channel with added Tween20 and without surfactant, respectively. For two droplets with a typical size, the increased deformability due

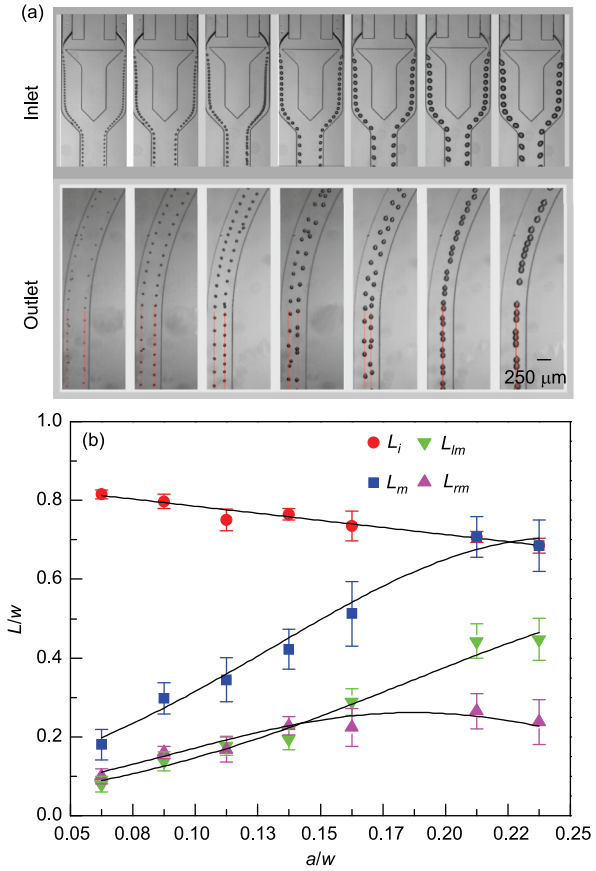

Figure 5 (Color online) (a) Experimental images of droplet distribution at the inlets and the corresponding outlets at Re = 0.13. The droplet sizes are 25, 35, 45, 55, 65, 85 and 95 μm successively. The red lines mark the equilibrium positions. (b) The lateral distance between the dual trains at the inlet L_i, the total migration distance L_m and the migration distance of the left train L_{lm} as well as the right train L_{rm} vary as functions of droplet sizes. The error bars reflect the uncertainty of measurements.

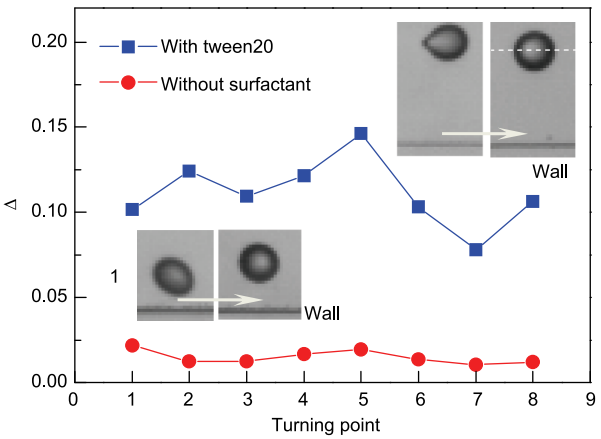

Figure 6 (Color online) The varying droplet deformation parameters with turning points along the DS channel at Re = 0.13 with Tween20 and without surfactant, respectively. Initial droplet sizes are identical as a = 65 μm. The insets show the typical droplets at the inlet (turning point 1) and the outlet (turning point 8) under the two conditions, respectively. The white arrows indicate the flow directions.

to Tween20 is reflected by the much greater and wavier droplet deformation. The deformation parameters under Tween20 laden condition are nearly ten-fold larger than those without surfactant. The visualized comparisons of droplet deformation are provided by the insets that show the droplet shapes and positions at the inlet and the outlet, respectively. Without added surfactant, the droplet shapes are near-round along all the channels. With Tween20, the shapes change from inclined-elliptical to pear shaped. This pear-like shape has been observed in non-inertial migration of vesicles in straight channels [48], reflecting the decreasing wall effect with inward migration.

3.1.4 *Detailed migration behaviour along the DS channel*

Though the experiments are performed at low Re, the effect of the DS channel is still observed. As shown in Figure 5, the dual droplet trains at the outlet are not completely symmetric with respect to the channel centerline, especially for larger droplets, and the focusing positions are off-axis. The focusing positions for different droplet sizes at Re from 0.13 to 0.38 are measured as almost the same, i.e., $x = 0.6w$, which differs from the centerline focusing happening in a straight channel [24,29]. More experimental demonstrations of the focusing are provided in Appendix (Figure a3). In this section, we thus inspect the detailed migration behavior along the DS channel to seek the explanation of this off-axis phenomenon. The total migration process of the dual droplet trains along the DS channel is exhibited in Figure 7(a). The numbers 1-8 are the turning points along the DS channel that indicate the flow sequence. The images with broader view are provided in Appendix (Figure a4). To show the varying migration clearly, the distributions of the dual trains at the turning points are successively grouped in Figures 7(b) and (c). The corresponding position functions for the three different droplet sizes are plotted against the turning points in Figure 7(d).

For small droplets, the DS channel can be considered as a long straight channel. The two trains still flow near the channel walls and keep nearly symmetric to the channel centerline at the outlet. For large droplets, the migration of each train varies greatly and the focusing of the two trains occurs in the half-loop before the outlet as denoted by turning point 7-8. Interestingly, in the inner loops denoted by turning point 3-6, migration distances of the two trains vary rarely with droplet sizes.

Though the inner loops only have limited contribution in reducing the lateral distance of two trains, they are mainly responsible for the off-axis phenomenon. The DS channel contains two anti-symmetric spiral channels and each spiral is integrated with four curved channels of different channel curvature radius R. The centrifugal force experienced by a droplet is inversely proportional to the square of curvature radius and proportional to the cube of droplet size. Therefore, in the channels with smaller R, the two droplet trains tend to synchronously migrate toward the inner wall. Larger droplet

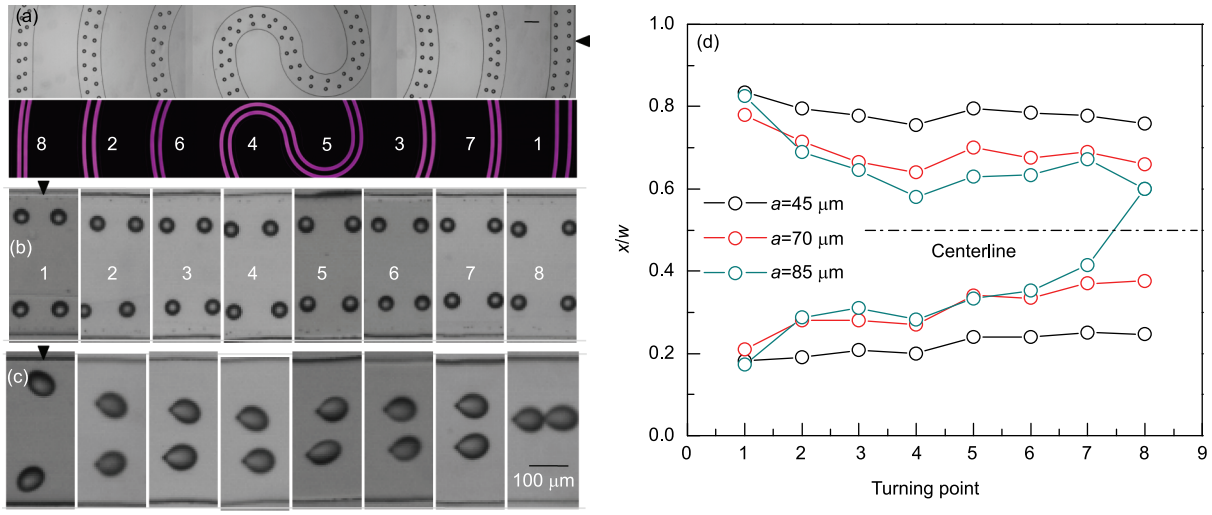

Figure 7 (Color online) (a) Experimental image depicts the total migrating process of the dual droplet trains along the whole DS channel for droplet size a = 65 μm. The composite image exhibits the dual trains at the turning points along the DS channel for droplet size a = 45 μm (b), and a = 85 μm (c). (d) The migrating trajectories along the DS channel for droplets with the three different sizes corresponding to (a)-(c). In (a), numbers 1-8 are the turning points and indicate the flow sequence. In (b), the numbers are corresponding to those in (a).

sizes intensify this synchronized shift and make it more distinct. As shown in Figure 7(d), the synchronized shift of the two trains in the innermost inverted S-shaped channel (turning point 4-5) almost offsets the accumulative shift of the first spiral channel. The accumulative shift in the second spiral channel then gives rise to the off-axis focusing position of the large droplets at the outlet.

3.2 Numerical: migration dynamics of single droplet in curved channels

Our experiments suggest that the equilibrium positions of droplets in the channel width vary with droplet sizes and deformability. We further conduct numerical simulations to obtain the size-dependent equilibrium positions. Figure 8 shows the curves of the accelerations in the channel width for droplet sizes a = 45, 68 and 90 μm. These droplet sizes are almost identical to the experimental set in Figure 7. The curve of the small droplet is anti-symmetric with respect to the centerline, suggesting two stable equilibrium positions at $x = 0.29w$ and $0.7w$, respectively. The equilibrium positions are almost the same with those in experiments shown in Figure 7(b) (turning point 8). This result agrees with the findings in a straight channel [25,48], indicating that the curved channel have little effect on small droplet. In contrast, the curves of larger droplets are asymmetric, reflecting the effect caused by the inner channel wall. The increasing droplet size enhances the effect induced by the left wall, resulting in a right shift of the equilibrium position. For even larger droplet, only one equilibrium position is obtained, which validates our experimental observations of droplet focusing in Figures 7(c) (turning point 8) and a3. More numerical results are provided in Appendix.

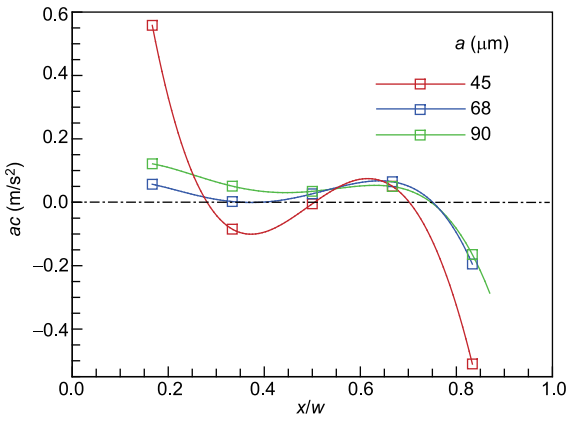

Figure 8 (Color online) The simulate curves of droplet accelerations for three different droplet sizes.

3.3 Application: sorting of the binary droplets

The employed microchip shows potential to fulfil the size-de-pendent sorting of the binary droplets in the low *Re* flows. Figure 9(a) describes the schematic of the sorting mechanism. Pre-sorting of the droplets near the walls can be completed by the intermediate sheath flow. After the pre-sorted droplets flowing through the DS microchannel, the large droplets ultimately focus at a deterministic position, i.e., $x = 0.6w$, while the small droplets remain in two ordered trains near the channel walls. To validate this mechanism, the experiments with coexisting large and small droplet are performed at $Re = 0.13$. The size-dependent sorting regime is obtained as expected, and the sorting and separation can be further completed using a bifurcate outlet with three side channels, as depicted in Figure 9(b).

This proposed low *Re* approach based on the lateral migration have many applications. For instance, with develop-

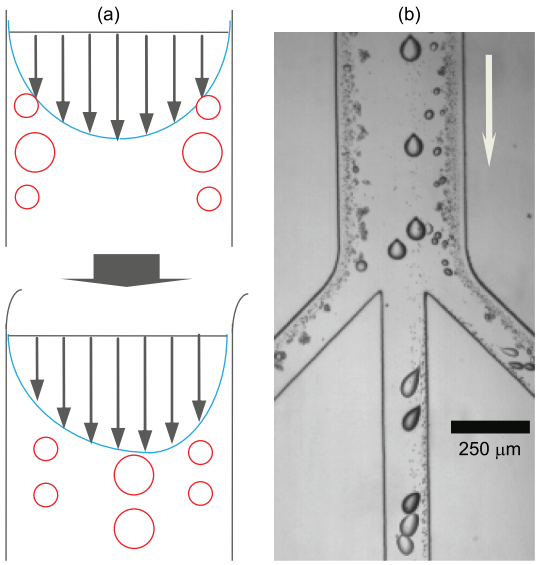

Figure 9 (Color online) (a) The schematic of the size-dependent separation regime. (b) Experimental image depicts the sorting of large droplets and the separation of smaller droplets. The droplet trajectories are visualized by an overlay of 20 frames.

ments of the all-aqueous systems [49], droplets with very low surface tension are gaining extensive interests [50,51]. Operating at low *Re* flow regime can avoid the mechanical damage on those fragile droplets. For certain bio-particles sensitive to flow shear stress [52], this low *Re* method is more suitable than inertial-driven methods.

4 Conclusion

In this work, we investigate the lateral migration of dual droplet trains in a double spiral microchannel at low *Re* numbers. We observe three migration modes with varying *Re* numbers, as disordered mode, size-dependent mode and size-independent mode. The size-dependent migration is intensively investigated and empirical formulas are established by relating the migration to *Re* numbers and droplet sizes. The effect of droplet deformability on the migration and the detailed migrating behavior along the double spiral channel are discussed. The increased deformability is found to enhance the migration. The double spiral structure poses accumulative effect on large droplets and gives rise to their off-axis focusing at the outlet. We also perform numerical simulations to investigate the droplet migration dynamics and yield results in qualitative agreement with the experiments. This proposed low *Re* approach based on this lateral migration could be a promising alternative to existing inertia-driven approaches especially for those deformable entities and susceptible bio-particles. Future efforts will focus on exploring the optimization of channel design, extending the sorting regime to smaller scales, and establishing the analytical formula to evaluate the wall effects in near-wall region.

This work was supported by the National Natural Science Foundation of China (Grant Nos. 11572334, 11272321 and 11402274).

1 A. B. Theberge, F. Courtois, Y. Schaerli, M. Fischlechner, C. Abell, F. Hollfelder, and W. T. S. Huck, Angew. Chim. Int. Ed. **49**, 5846 (2010).
2 T. P. Lagus, and J. F. Edd, J. Phys. D-Appl. Phys. **46**, 114005 (2013).
3 X. Chen, and G. Q. Hu, Adv. Mech. **45**, 201503 (2015).
4 Z. Li, G. H. Hu, Z. L. Wang, Y. B. Ma, and Z. W. Zhou, Phys. Fluids **25**, 072103 (2013).
5 H. Song, D. L. Chen, and R. F. Ismagilov, Angew. Chem. Int. Ed. **45**, 7336 (2006).
6 E. W. M. Kemna, L. I. Segerink, F. Wolbers, I. Vermes, and A. van den Berg, Analyst **138**, 4585 (2013).
7 M. Chabert, and J. L. Viovy, Proc. Natl. Acad. Sci. **105**, 3191 (2008).
8 Z. Cao, F. Chen, N. Bao, H. He, P. Xu, S. Jana, S. Jung, H. Lian, and-C. Lu, Lab Chip **13**, 171 (2013).
9 M. Hein, M. Moskopp, and R. Seemann, Lab Chip **15**, 2879 (2015).
10 K. Ahn, C. Kerbage, T. P. Hunt, R. M. Westervelt, D. R. Link, and D. A. Weitz, Appl. Phys. Lett. **88**, 024104 (2006).
11 M. P. MacDonald, G. C. Spalding, and K. Dholakia, Nature **426**, 421 (2003).
12 T. Ohashi, H. Kuyama, K. Suzuki, and S. Nakamura, Anal. Chim. Acta **612**, 218 (2008).
13 J. Shi, D. Ahmed, X. Mao, S. C. S. Lin, A. Lawit, and T. J. Huang, Lab Chip **9**, 2890 (2009).
14 J. DuBose, X. Lu, S. Patel, S. Qian, S. W. Joo, and X. Xuan, Biomicrofluidics **8**, 014101 (2014).
15 X. Xuan, J. Zhu, and C. Church, Microfluid Nanofluid **9**, 1 (2010).
16 D. Di Carlo, D. Irimia, R. G. Tompkins, and M. Toner, Proc. Natl. Acad. Sci. **104**, 18892 (2007).
17 T. M. Geislinger, and T. Franke, Adv. Colloid Interface Sci. **208**, 161 (2014).
18 D. Di Carlo, J. F. Edd, K. J. Humphry, H. A. Stone, and M.Toner, Phys. Rev. Lett. **102**, 094503 (2009).
19 C. Liu, G. Hu, X. Jiang, and J. Sun, Lab Chip **15**, 1168 (2015).
20 H. Amini, W. Lee, and D. Di Carlo, Lab Chip **14**, 2739 (2014).
21 C. Liu, C. Xue, J. Sun, and G. Hu, Lab Chip **16**, 884 (2016).
22 H. L. Goldsmith, and S. G. Mason, Nature **190**, 1095 (1961).
23 H. L. Goldsmith, and S. G. Mason, J. Colloid Sci. **17**, 448 (1962).
24 A. Karnis, H. L. Goldsmith, and S. G. Mason, Nature **200**, 159 (1963).
25 X. Chen, C. Xue, L. Zhang, G. Hu, X. Jiang, and J. Sun, Phys. Fluids **26**, 112003 (2014).
26 C. E. Chaffey, H. Brenner, and S. G. Mason, Rheol Acta **4**, 64 (1965).
27 H. Mohammadigoushki, and J. J. Feng, Phys. Rev. Lett. **109**, 084502 (2012).
28 A. Karnis, and S. G. Mason, J. Colloid Interface Sci. **24**, 164 (1967).
29 S. A. E. E. D. Mortazavi, and G. R. T. A. R. Tryggvason, J. Fluid Mech. **411**, 325 (2000).
30 M. Shapira, and S. Haber, Int. J. Multiphase Flow **14**, 483 (1988).
31 L. Y. Zeng, S. Balachandar, and P. Fischer, J. Fluid Mech. **536**, 1 (2005).
32 H. Maenaka, M. Yamada, M. Yasuda, and M. Seki, Langmuir **24**, 4405 (2008).
33 T. M. Geislinger, B. Eggart, S. Braunmüller, L. Schmid, and T. Franke, Appl. Phys. Lett. **100**, 183701 (2012).
34 T. M. Geislinger, and T. Franke, Biomicrofluidics **7**, 044120 (2013).
35 J. Sun, M. Li, C. Liu, Y. Zhang, D. Liu, W. Liu, G. Hu, and X. Jiang, Lab Chip **12**, 3952 (2012).
36 A. A. S. Bhagat, S. S. Kuntaegowdanahalli, and I. Papautsky, Lab Chip **8**, 1906 (2008).
37 L. Frenz, J. Blouwolff, A. D. Griffiths, and J. C. Baret, Langmuir **24**, 12073 (2008).

38 J. Hong, M. Choi, J. B. Edel, and A. J. deMello, Lab Chip **10**, 2702 (2010).
39 D. C. Duffy, J. C. McDonald, O. J. A. Schueller, and G. M. Whitesides, Anal. Chem. **70**, 4974 (1998).
40 S. Popinet, J. Comp. Phys. **228**, 5838 (2009).
41 X. Chen, and V. Yang, J. Comp. Phys. **269**, 22 (2014).
42 A. P. Sudarsan, and V. M. Ugaz, Lab Chip **6**, 74 (2006).
43 A. P. Sudarsan, and V. M. Ugaz, Proc. Natl. Acad. Sci. **103**, 7228 (2006).
44 C. A. Stan, A. K. Ellerbee, L. Guglielmini, H. A. Stone, and G. M. Whitesides, Lab Chip **13**, 365 (2013).
45 G. I. Taylor, Proc. R. Soc. A-Math. Phys. Eng. Sci. **146**, 501 (1934).
46 P. C. H. Chan, and L. G. Leal, J. Fluid Mech. **92**, 131 (1979).
47 L. G. Leal, Annu. Rev. Fluid Mech. **12**, 435 (1980).
48 G. Coupier, B. Kaoui, T. Podgorski, and C. Misbah, Phys. Fluids **20**, 111702 (2008).
49 S. Hardt, and T. Hahn, Lab Chip **12**, 434 (2012).
50 Y. Song, A. Sauret, and H. Cheung Shum, Biomicrofluidics **7**, 061301 (2013).
51 U. Shimanovich, Y. Song, J. Brujic, H. C. Shum, and T. P. J. Knowles, Macromol. Biosci. **15**, 501 (2015).
52 L. F. Li, C. Xiang, and K. R. Qin, Biomech. Model Mechanobiol. **14**, 979 (2015).
53 J. U. Brackbill, D. B. Kothe, and C. Zemach, J. Comp. Phys. **100**, 335 (1992).
54 X. Chen, D. Ma, V. Yang, and S. Popinet, Atomiz. Spr. **23**, 1079 (2013).

Appendix A1 Governing equations and numerical methods

The governing conservation equations for the incompressible and variable-density flow with surface tension are [40]

$$\partial_t \rho + \nabla \cdot (\rho u) = 0, \tag{a1}$$

$$\rho(\partial_t u + u \cdot \nabla u) = -\nabla p + \nabla \cdot (2\mu D) + \sigma\kappa\delta_s n, \tag{a2}$$

$$\nabla \cdot u = 0, \tag{a3}$$

where $\boldsymbol{u}$ is the velocity vector, ρ the fluid density, μ the dynamic viscosity, and $\boldsymbol{D}$ the deformation tensor defined as $D_{ij} = (\partial_i u_j + \partial_j u_i)/2$. The Dirac delta function δ_s indicates the fact that the interfacial tension, σ, is concentrated on the interface. The radius of curvature of the interface is denoted by κ, and $\boldsymbol{n}$ is the unit outward vector normal to the interface [40].

The volume-of-fluid (VOF) function $c(\boldsymbol{x}, t)$ is introduced to trace the two-fluid interface. $c(\boldsymbol{x}, t)$ is defined as the volume fraction of a given fluid in each cell of the computational mesh. The density and viscosity can thus be written as:

$$\rho(c) \equiv c\rho_1 + (1-c)\rho_2, \tag{a4}$$

$$\mu(c) \equiv c\mu_1 + (1-c)\mu_2, \tag{a5}$$

where ρ_1, ρ_2 and μ_1, μ_2 are the densities and viscosities of the first and second fluids, respectively. In addition, according to mass continuity, the advection equation is given as:

$$\partial_t c + \nabla \cdot (cu) = 0. \tag{a6}$$

The staggered temporal discretization of the volume-fraction/density and pressure is applied and leads to a scheme which is second-order accurate in time. The classical time-splitting projection method is used, which requires the solution of a Poisson equation. In order to improve numerical efficiency and robustness, the discretized momentum equation is recast as Helmholtz-type equation that can be solved by an improved multi-level Poisson solver. The resulting Crank-Nicholson discretization of the viscous terms is second-order accurate. Spatial discretization is achieved using graded octree partitioning in three dimensions. All the variables are collocated at the center of each discretized cubic volume. Consistent with the finite-volume formulation, variables are interpreted as volume-averaged values for each cell. A piecewise-linear geometrical VOF scheme generalized for octree spatial discretization is used to solve the advection equation for the volume fraction [53]. Since the original Continuum-Surface-Force (CSF) approach [53] suffers from problematic parasitic currents, the combination of a balanced-force surface tension discretization and a height-function curvature estimation is used to circumvent the problem. The CFL number is set to be 0.8 for all the simulations to ensure the overall numerical stability.

The gradient-based adaptive mesh refinement (AMR) method is used for the volume fraction. Adequate mesh refinement is guaranteed along the entire interface where the volume fraction has gradients. Due to the confinement of the channel walls, thin films between the walls and droplet exist when droplets are close to the walls. The efficient thickness-based refinement methods [41] are applied to refine the thin regions. In Figure a2, typical grid on the interface of a droplet near the wall is shown. The local refinement allows fine cells only near the wall to avoid refinement of the entire interface, thus reduce numerical cost dramatically. These numerical methods have been validated in high-fidelity numerical simulation of impinging jet atomization [54] and droplet deformation and migration in straight microchannels [25].

The effects of curvature radius and the interfacial tension on droplet migration are also numerically investigated (Figure a5). The droplet size is fixed as $a = 90$ μm. For that the centrifugal force is inversely proportional to the square of channel radius, the droplet acceleration is expected to decrease with increasing channel radius. Nevertheless, small radius give rises to limited channel length that just supports little time for droplet migration. The equilibrium position only shifts a little to the centerline with channel radius decreasing. In addition, as the interfacial tension decreases, the acceleration of droplet migration increases appreciably. This gives the explanation that the increased deformability enhances the droplet migration as suggested in Figures 3(a) and 6 in the main text. The equilibrium position is found to move slightly toward the right wall as the interfacial tension decreases.

Appendix A2 Figures

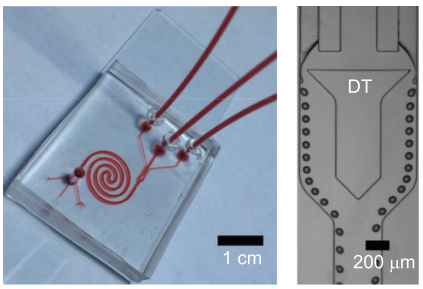

Figure a1 (Color online) The assembled microchip used in the experiments and the experimental snapshot showing the generation of the dual droplet trains in the double T structure.

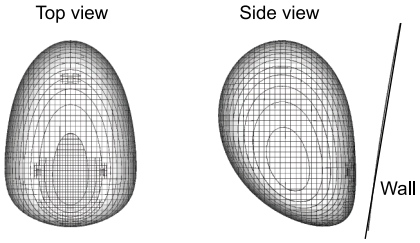

Figure a2 Typical grid on the interface of a droplet when it flows near the channel wall. Both the top and side views are displayed. As shown distinctly in side view, the local refinement allows fine cells only near the wall. This avoids refinement of the entire interface, thus to reduce numerical cost dramatically.

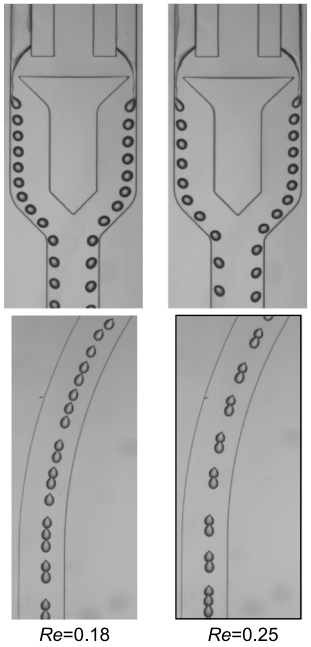

Figure a3 Experimental snapshots of droplet distribution at the inlets and the corresponding outlets at Re = 0.18 and 0.25, respectively. The droplet sizes are adjusted to be equal, about a = 96 μm. At the outlet, the focusing positions are measured as about $x = 0.59w$. Compared with $x = 0.6w$ at Re = 0.13, the discrepancy is very small (~$0.01w$).

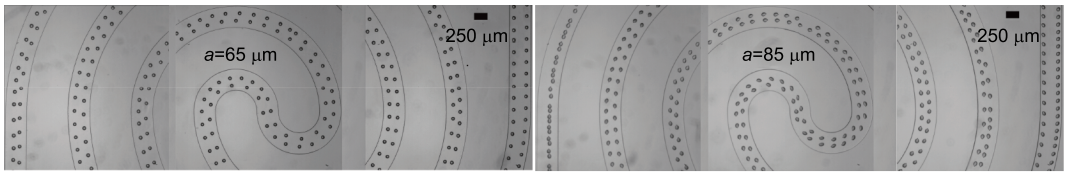

Figure a4 Experimental image with broad view depicts the migration process of the dual droplet trains along the whole DS microchannel for a = 65 and 85 μm at Re = 0.13, respectively.

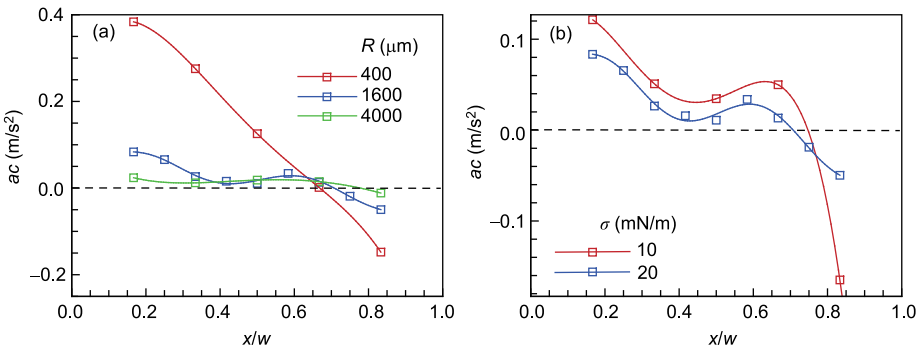

Figure a5 (Color online) The simulate curves of the droplet accelerations for (a) three different curvature radius, and (b) two different droplet surface tension. The droplet size is fixed as a = 90 μm.